**Citation**
Fielding, I. and Johnson, S. and Zi, J. and Sheppard, S. and Rasmussen, B. 2018. Neighbouring orogenic gold deposits may be the products of unrelated mineralizing events. Ore Geology Reviews. 95: pp. 593-603. http://doi.org/10.1016/j.oregeorev.2018.03.011

Ore Geology Reviews 95 (2018) 593–603

Contents lists available at ScienceDirect

Ore Geology Reviews

journal homepage: www.elsevier.com/locate/oregeorev

# Neighbouring orogenic gold deposits may be the products of unrelated mineralizing events

Imogen O.H. Fielding[a,*], Simon P. Johnson[b], Jian-Wei Zi[a], Stephen Sheppard[a,c], Birger Rasmussen[d]

[a] Department of Applied Geology, Curtin University, Kent Street, Bentley, Western Australia 6102, Australia
[b] Geological Survey of Western Australia, 100 Plain Street, East Perth, Western Australia 6004, Australia
[c] Prime Geological Mapping, PO Box 3014, Carlisle South, Western Australia, 6101, Australia
[d] School of Earth Sciences, The University of Western Australia, Perth, Western Australia 6009, Australia

ARTICLE INFO

*Keywords:*
Geochronology
Xenotime
Baddeleyite
SHRIMP
Gold
Capricorn Orogen

ABSTRACT

Models for exploration targeting are often developed by assessing known gold deposits in a region, and targeting similar geological features such as geochemical anomalies, favourable host rocks or structural settings with the assumption that they represented the footprint of the mineralizing event. Belvedere and Paulsens are gold deposits with similar characteristics located in the Wyloo Inlier in the north Capricorn Orogen, Western Australia. Gold at both deposits is hosted in quartz–carbonate–sulfide veins within mafic intrusive rock. Prior to this study they were thought to have formed during the same hydrothermal mineralizing event. At Belvedere, in situ baddeleyite geochronology yields a weighted mean $^{207}Pb*/^{206}Pb*$ crystallization age of 2082 ± 30 Ma for the Belvedere dolerite which hosts the ore body. Xenotime intergrown with ore-stage alteration minerals, and encased in arsenopyrite, yielded a $^{207}Pb*/^{206}Pb*$ date of 1681 ± 9 Ma, interpreted to represent the timing of hydrothermal activity related to gold mineralization at the Belvedere deposit. Despite the similarities between the two deposits, our results indicate that they underwent different geological histories with primary gold mineralization at Paulsens occurring at c. 2400 Ma, pre-dating both the Belvedere dolerite and mineralization within the dolerite. Furthermore, field relationships show that the suite of dolerite dykes to which the Belvedere dolerite belongs, crosscut gold mineralization at Paulsens. The in situ U–Pb geochronology techniques employed here, combined with field relationships, have led to a better understanding on age constraints of gold deposition in the Wyloo Inlier and challenges the assumption that orogenic deposits in a given region probably formed during a single mineralizing event.

## 1. Introduction

Gold deposits within a given geological terrane that exhibit similar characteristics are commonly thought to have formed due to the same geological processes during the same hydrothermal event (Cheng, 2008; Groves et al., 1998). This is particularly apparent in orogenic gold systems as they form during collisional or accretionary orogenies resulting in numerous gold deposits of varying size that form linear trends along major faults associated with crustal boundaries (Bierlein et al., 2006; Goldfarb et al., 2001; Groves et al., 2005). Since faults and major structures can act as fluid pathways (Hronsky et al., 2012; Korsch and Doublier, 2016), it is possible that remobilization or new mineralizing events could be superimposed along the same system. Therefore, without knowing the absolute ages of host rocks and gold mineralization at individual deposits in a region, it is not obvious as to whether they are all a result of a single mineralizing event or were formed during multiple, superimposed events. In this contribution, we examine the timing of gold mineralization at two similar, closely spaced deposits in the Wyloo Inlier in Western Australia to investigate whether they are the result of a single or multiple mineralizing events.

The Belvedere and Paulsens gold deposits are located in the Wyloo Inlier situated on the southern margin of the Pilbara Craton in Western Australia (Fig. 1; Thorne and Trendall, 2001). The Paulsens deposit is significantly larger than Belvedere with a total endowment of 1.1 Moz of gold (Blockley, 1971; Fielding et al., 2017). The Belvedere deposit had 454 oz of gold extracted during the 1930 s (Blockley, 1971) and has a remaining resource of 31,000 oz of contained gold (Northern Star Resources Limited, 2015a). The deposits are 6.5 km apart and historically were interpreted as vein-hosted gold deposits associated with the 1820–1770 Ma Capricorn Orogeny (Thorne and Trendall, 2001).

* Corresponding author.
*E-mail address:* imogen.fielding@postgrad.curtin.edu.au (I.O.H. Fielding).

https://doi.org/10.1016/j.oregeorev.2018.03.011
Received 9 January 2018; Received in revised form 8 March 2018; Accepted 13 March 2018
Available online 14 March 2018

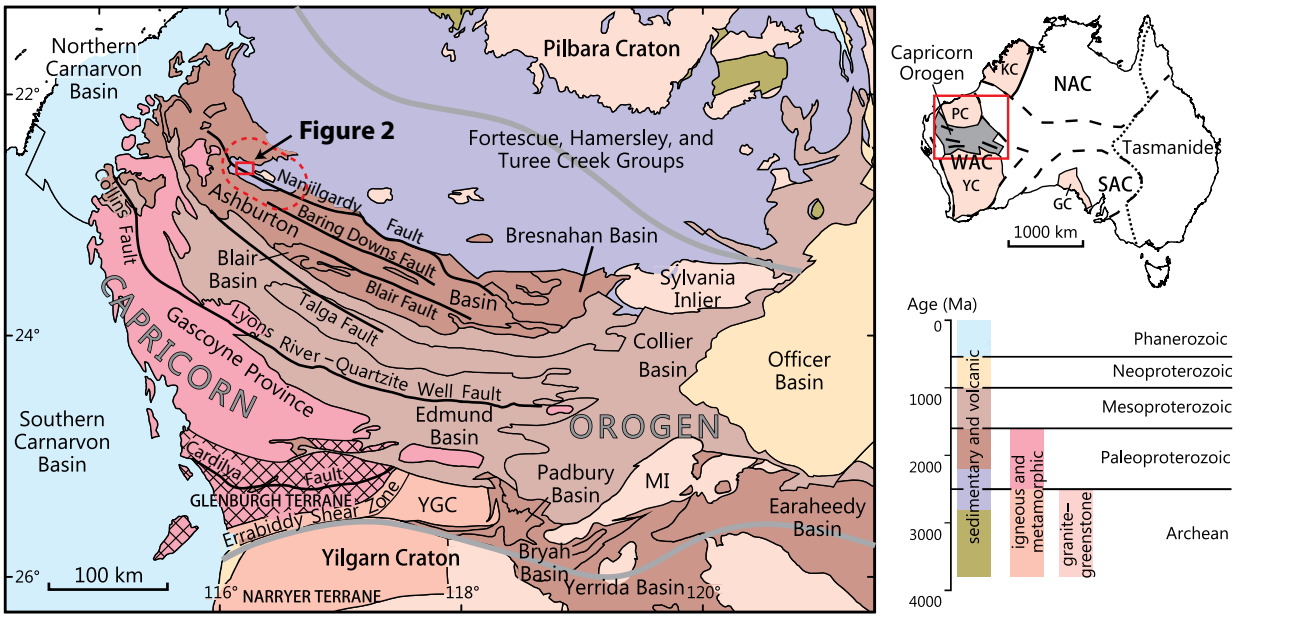


**Fig. 1.** Location of the Capricorn Orogen in Western Australia, showing location of the Wyloo Inlier (dashed red ellipse) and inset location for Fig. 2. Abbreviations: GC = Gawler Craton, KC = Kimberley Craton, MI = Marymia Inlier, NAC = North Australian Craton, PC = Pilbara Craton, SAC = South Australian Craton, WAC = West Australian Craton, YC = Yilgarn Craton, YGC = Yarlarweelor Gneiss Complex (after Johnson et al., 2013).

Originally it was thought the Capricorn Orogeny represented the collision between the Pilbara and Yilgarn cratons (Tyler and Thorne, 1990) but is now known to have been an episode of intracratonic reworking (Johnson et al., 2017; Sheppard et al., 2010). Both deposits share the main characteristics of orogenic gold deposits: 1) mineralization comprises quartz–carbonate–sulfide veins; 2) the host rocks are metamorphosed to epidote-actinolite greenschist facies (White et al., 2014); 3) ore-stage alteration assemblages consist of muscovite, carbonate and quartz; 4) the deposits contain native gold (Fielding et al., 2017; Norum, 2005; Owen, 2000), and 5) the deposits are spatially associated with a crustal-scale fault. An additional feature common to the deposits is that mafic intrusive rocks host the auriferous quartz–carbonate–-sulfide veins. Despite these similarities, the suite of dolerite dykes which hosts the Belvedere deposit post-date, and cross cut gold mineralization at Paulsens, suggesting that gold mineralization at the two deposits was not synchronous.

Published data and descriptions of the Belvedere deposit are limited to brief mentions in open-file company reports held by the Department of Mines, Industry, Regulation and Safety and in Geological Survey of Western Australia reports (e.g., Blockley, 1971; Forman, 1938; Marston, 1979; Thorne and Trendall, 2001). Here we present new data, including more detailed field relationships and in situ U–Pb SHRIMP geochronology for the Belvedere gold deposit, to determine the age of the host rocks to gold mineralization and the timing of hydrothermal activity related to gold formation. These data are then compared to published information from the Paulsens gold deposit (e.g., Fielding et al., 2017) to demonstrate that gold deposits in close proximity, with similar appearances, may form at separate times and in different tectonic settings.

## 2. Geological setting

The Wyloo Inlier is situated in the northern part of the Paleoproterozoic Capricorn Orogen on the southern margin of the Pilbara Craton (Fig. 1). The Capricorn Orogen has a complex tectonothermal evolution which includes at least seven tectonic events over approximately 1.6 billion years (Cawood and Tyler, 2004; Johnson et al., 2011, 2013; Korhonen et al., 2017; Martin and Morris, 2010; Sheppard et al., 2005, 2007). The first two tectonic events (the Ophthalmia Orogeny and the Glenburgh Orogeny) mark the amalgamation of the West Australian Craton. During the 2215–2145 Ma Ophthalmia Orogeny (Johnson et al., 2011; Rasmussen et al., 2005) the Glenburgh Terrane collided with the Pilbara Craton. Subsequently, during the 2005–1950 Ma Glenburgh Orogeny, the combined Pilbara Craton – Glenburgh Terrane collided with the Yilgarn Craton (Johnson et al., 2011; Occhipinti et al., 2004; Sheppard et al., 2004). Once assembled, the West Australian Craton experienced over a billion years of intracratonic reworking and reactivation during the 1820–1770 Ma Capricorn Orogeny (Cawood and Tyler, 2004; Sheppard et al., 2010), the 1680–1620 Ma Mangaroon Orogeny (Sheppard et al., 2005), the 1320–1170 Ma Mutherbukin Tectonic Event (Korhonen et al., 2017), the 1030–955 Ma Edmundian Orogeny (Martin and Thorne, 2004; Sheppard et al., 2007), and the c. 570 Ma Mulka Tectonic Event (Johnson et al., 2013).

Within the Wyloo Inlier, Archean basement rocks of the Pilbara Craton are overlain by Archean to Paleoproterozoic metasedimentary and metavolcanic rocks of the Fortescue Group, Hamersley Group, Turee Creek Group, Shingle Creek Group and the Paleoproterozoic Ashburton Formation of the Wyloo Group (Seymour et al., 1988; Thorne and Trendall, 2001). The rocks throughout the Wyloo Inlier are overprinted by regional-scale epidote-actinolite greenschist facies metamorphism (White et al., 2014), and intruded by at least five suites of mafic dykes and sills. Of these dyke suites, only the oldest and youngest have been dated at, respectively, 2701 ± 11 Ma (Fielding et al., 2017) and 753 ± 11 Ma (Wingate et al., 2017a).

Deep crustal seismic reflection imaging across the Capricorn Orogen identified five crustal-scale faults which show a spatial relationship with gold occurrences (Johnson et al., 2013). In the northern Capricorn Orogen, a second order structure of the Nanjilgardy Fault, known as the Hardey Fault, is spatially associated with the Belvedere deposit (Fig. 2) and is linked to c. 2400 and 1680 Ma gold mineralizing events at Paulsens (Fielding et al., 2017).

## 3. Local geology

The Belvedere gold deposit is located in the core of the Wyloo Inlier within the Mount Roe Basalt (Fig. 2; Thorne and Trendall, 2001). The local stratigraphy at Belvedere includes vesicular basalt, polymictic conglomerate, sandstone and siltstone (Fig. 3).

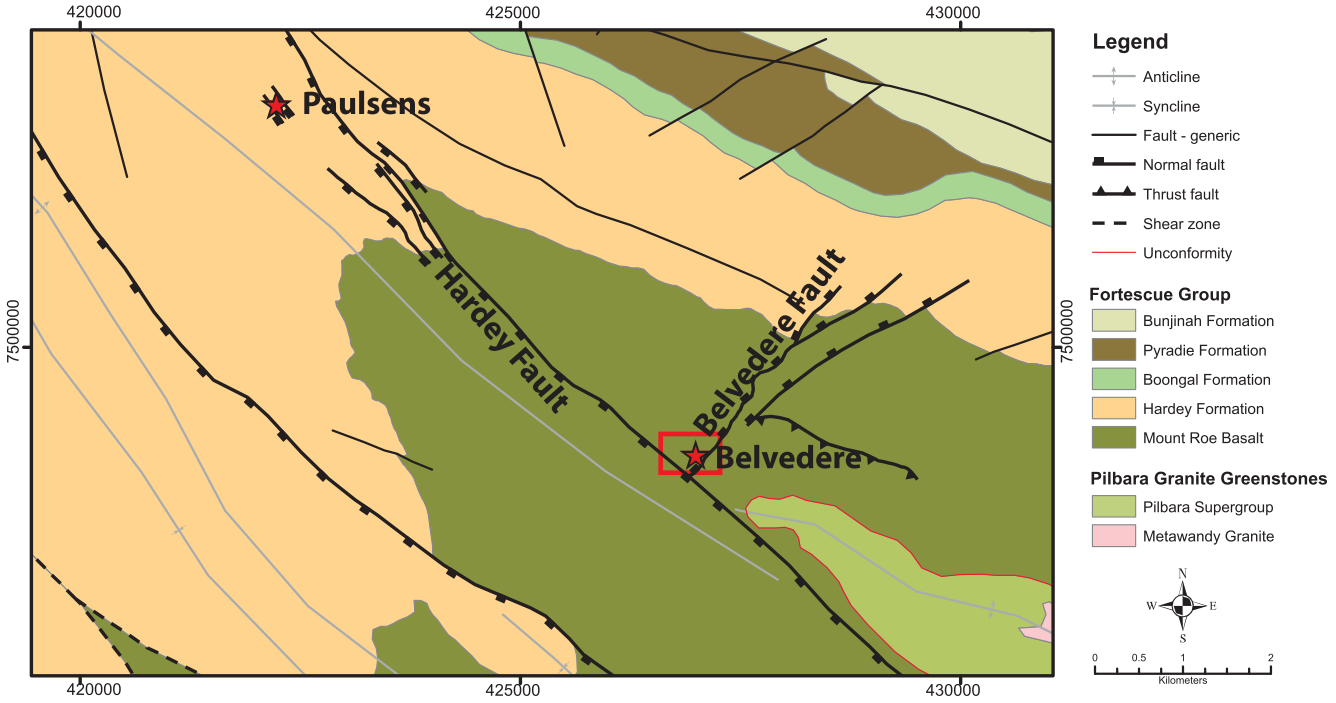


**Fig. 2.** Geology map of the northern part of the Wyloo Inlier (courtesy of Northern Star Resources Ltd. Pty) showing the location of the Belvedere and Paulsens Deposits. Coordinates are in meters (MGA94 zone 50). Red box shows the location of Fig. 3.

At least four low-grade deformation events have affected the rocks of the Wyloo Inlier, during which two widespread cleavages formed, followed by fault reactivation along pre-existing crustal-scale faults (Krapež, 1999; Thorne and Seymour, 1991). The first event ($D_1$) caused regional-scale, epidote-actinolite greenschist facies metamorphism (White et al. 2014) accompanied by tight to upright folds, a penetrative, spaced, axial planar cleavage ($S_1$) with an average orientation of 320/85SW (Fielding et al., 2017), and is thought to be related to the 2215–2145 Ma Ophthalmia Orogeny (Tyler and Thorne, 1990). The second event ($D_2$), is characterized by lower greenschist facies metamorphism with the growth of chlorite-sericite-muscovite in pelitic and semi-pelitic rocks and chlorite-amphibole in mafic and mafic volcanoclastic rocks (Tyler, 1991; Smith et al., 1982). The $D_2$ event is near-coaxial to $D_1$ and is linked to the 1820–1770 Ma Capricorn Orogeny (Thorne and Seymour, 1991). It caused tightening of the $F_1$ folds, attenuation of northern limbs to form shear zones up to 50 m wide, and

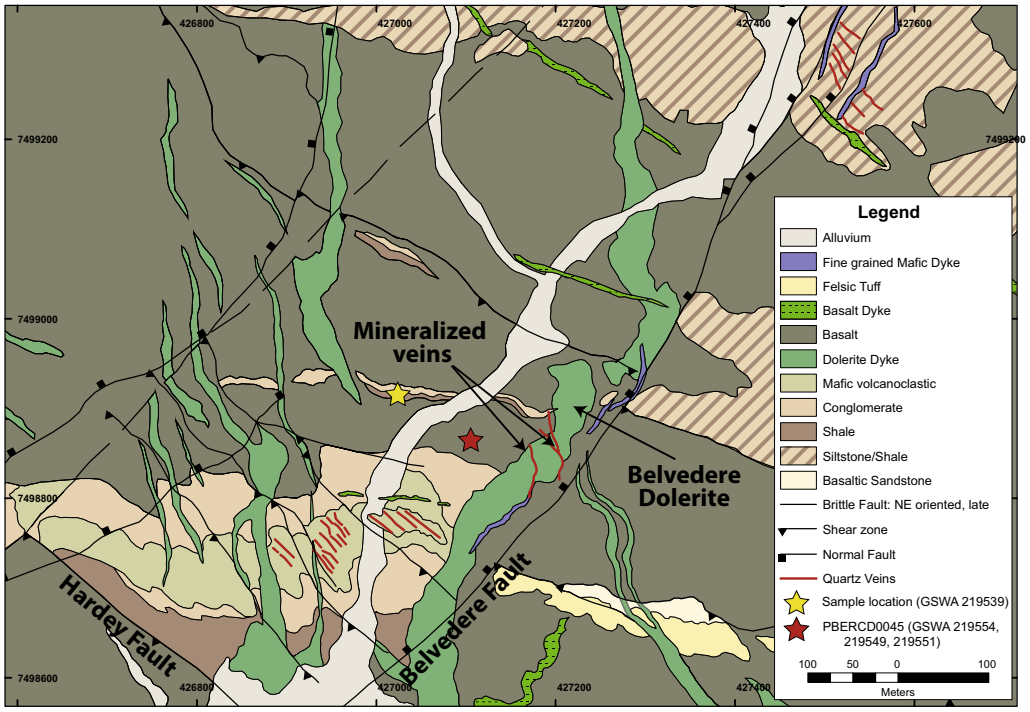


**Fig. 3.** Local geology map of the Belvedere deposit showing location of the samples, Belvedere dolerite, mineralized quartz–carbonate–arsenopyrite veins and Belvedere and Hardey Faults. Coordinates are in meters (MGA94 zone 50).

development of a spaced cleavage ($S_2$) with an average orientation of 305/85SW (Fielding et al., 2017). $S_1$ and $S_2$ can be difficult to differentiate in the field due to their sub-parallel nature. $D_3$ and $D_4$ are characterized by WNW-trending dextral followed by sinistral strike-slip reactivation (Krapež, 1999) of the Nanjilgardy Fault and its subsidiary structures, including the Hardey Fault, during the final stages of the Capricorn Orogeny (Krapež, 1999; Thorne and Seymour, 1991) and early stages of the 1680–1620 Ma Mangaroon Orogeny (Fielding et al., 2017).

Proximal to the Belvedere ore body there are three suites of mafic intrusive rocks. An early folded gabbroic dyke with an igneous crystallization age of 2734 ± 14 Ma (Wingate et al., 2017a,b) intrudes the Mount Roe Basalt immediately north of the Belvedere deposit and is crosscut by northwest-trending $S_1$ and $S_2$ fabrics. Two later suites of dolerite dykes strike north and northwest and crosscut the gabbro. The relationship between the two younger suites of dolerite dykes is not clear, and currently no geochronological data are available. The dolerites are generally undeformed, although the north-striking dolerite dykes are locally kinked with a spaced cleavage preserved in the deformed zones.

## 4. Deposit description

The Belvedere orebody is hosted by a 30 m-thick, north-striking, ~40°-west dipping, fine- to medium-grained dolerite dyke informally known as the Belvedere dolerite. The Belvedere dolerite is largely undeformed, although it is foliated at the contact with the mineralized quartz–carbonate–arsenopyrite veins. Overall, it has a northerly strike but close to the orebody it intrudes along the northeast-striking Belvedere fault for approximately 500 m (Fig. 3). Sinistral strike-slip reactivation of the Belvedere fault resulted in the formation of two Rieldel shear zones and associated auriferous quartz–carbonate–arsenopyrite veins, surrounded by muscovite-ankerite-quartz ± rutile ± albite alteration (Norum, 2005). The mineralized quartz–carbonate–arsenopyrite veins are 2–12 m wide with native gold forming irregular inclusions up to 150 μm by 20 μm (Fig. 4A) within euhedral arsenopyrite crystals < 2 mm in diameter. Metallurgical test work indicates most of the gold occurs as free gold that is not bound within the arsenopyrite crystal lattice (Owen, 2000). Small amounts of gold mineralization are also present in quartz–carbonate–arsenopyrite veins occurring sporadically within the Belvedere Fault itself.

There are currently no reliable age constraints on mineralization at Belvedere. Lead isotope ratios of galena suggest that mineralization occurred during the late Proterozoic (Richards et al., 1981), although these conclusions are ambiguous because the data plot away from the model III growth curve of Cumming and Richards (1975). Thorne and Trendall (2001) attributed gold mineralization at Belvedere to emplacement of post-Fortescue Group veins, linking their formation to the 1820–1770 Ma Capricorn Orogeny; however, this has not been verified by geochronology.

## 5. Geochronology methods

Four samples, (Fig. 3) including three from diamond drill core PBERCD0045 (MGA 94 zone 50 427093E 7498864N) and one from a surface outcrop (MGA 94 zone 50 427026E 7498915N), were analysed to determine the igneous crystallization age of the Belvedere dolerite, and the age of hydrothermal activity and associated gold mineralization. Polished thin sections were examined by optical and scanning electron microscope (SEM) to identify minerals suitable for in situ SHRIMP geochronology, such as monazite, xenotime and baddeleyite. Once identified, the minerals were drilled out of the polished thin section using a 2–3 mm hollow core drill bit and cast into a 25 mm epoxy SHRIMP mount. The in situ dating method preserves the textural context of minerals being dated, allowing the significance of the date obtained to be better understood. Reference materials xenotime MG1 (Fletcher et al., 2004), Xeno1 and Xeno2 (Stern and Rayner, 2003) and baddeleyite Phalaborwa (Heaman and LeCheminant, 1993) were placed on a separate SHRIMP mount which was cleaned and gold coated with the sample mounts for each analytical session.

Xenotime and baddeleyite were analysed for U, Th and Pb isotopes using the SHRIMP II instrument at the John de Laeter Centre at Curtin University in Perth, Western Australia. In situ small spot analysis of xenotime followed established procedures outline by Fletcher et al. (2004). Data were collected over several analytical sessions using varying parameters which are summarised in Table 1. The appendix describes the analytical procedures in detail.

## 6. Sample details and results

All age calculations are derived from 204-corrected $^{207}Pb*/^{206}Pb*$ ratios (Pb* denotes radiogenic lead). Up to 2% common lead and 10% discordance for individual analyses are tolerated unless mentioned below. Data in tables and plots for individual analyses are quoted with 1σ uncertainties; weighted mean $^{207}Pb*/^{206}Pb*$ dates are quoted with 95% confidence intervals.

### 6.1. Baddeleyite

#### 6.1.1. GSWA 219544: Belvedere dolerite

A medium- to coarse-grained portion of the Belvedere dolerite was sampled from diamond drill hole PBERCD0045, between 54.25 and 54.60 m, to determine the emplacement age of the dolerite that hosts the mineralized quartz–carbonate–arsenopyrite veins. Euhedral baddeleyite crystals up to 150 μm long (Fig. 4B) are common throughout the sample. Many of the baddeleyite crystals have thin fringes of very fine-grained zircon (Fig. 4B), although in some cases the baddeleyite crystal has been entirely replaced by crystalline zircon with abundant very-fine grained inclusions (Fig. 4C). Attempts were made to date the zircon fringes and zircon pseudomorphs but all analyses are > 10% discordant.

Fifteen analyses were made on 10 baddeleyite crystals with U and Th concentrations ranging from, 73 to251 ppm and 3 to46 ppm, respectively. Care was taken to ensure the analysis spot did not overlap the zircon fringes. Two analyses with > 2% common lead and two younger statistical outliers, possibly due to Pb-loss, were excluded from the age determination. Seven of the analyses are > 10% discordant likely due to the crystal orientation effect of baddeleyite which may bias the $^{206}Pb*/^{238}U$ ratios (Wingate and Compston, 2000). However, the $^{207}Pb*/^{206}Pb*$ ratios show good consistency and are considered reliable in the age determination. Eleven analyses yield a weighted mean $^{207}Pb*/^{206}Pb*$ date of 2082 ± 30 Ma (MSWD = 0.96; Table 2; Fig. 5A), interpreted as the crystallization age of the Belvedere dolerite.

### 6.2. Xenotime

#### 6.2.1. GSWA 219549: Auriferous quartz–carbonate–arsenopyrite vein

A sample of the mineralized quartz–carbonate–arsenopyrite vein with assay results of 1.15 ppm Au, was sampled from diamond drill hole PBERCD0045 between 77.39 and 77.68 m. The sample is composed predominantly of quartz with lesser amount of ore-stage alteration including very fine-grained muscovite–carbonate–rutile and euhedral arsenopyrite crystals < 1 mm long. Xenotime is mostly anhedral and commonly contains laths of muscovite (Fig. 4D) indicating that xenotime growth occurred during ore-stage hydrothermal activity.

Thirteen analyses were conducted on 8 xenotime crystals with U and Th concentrations ranging from 462 to2611 ppm and 49 to 64 ppm, respectively. One analysis yielded > 1% common Pb, and was excluded from the age determination. The remaining 12 analyses give a weighted mean $^{207}Pb*/^{206}Pb*$ date of 1682 ± 13 Ma (MSWD = 0.59; Table 3, Fig. 5B) which is interpreted to represent the timing of hydrothermal activity related to ore-stage alteration and associated gold

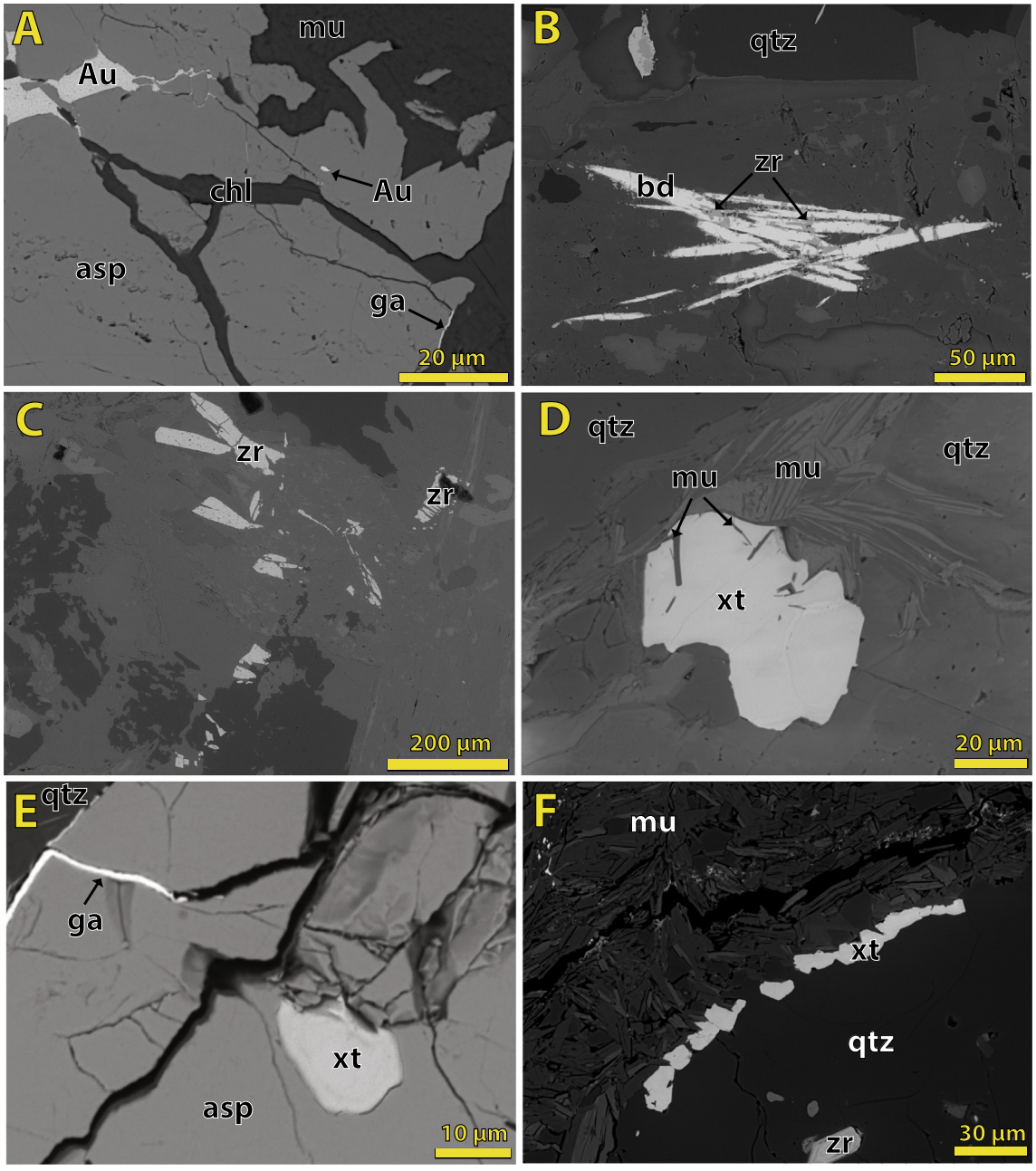


**Fig. 4.** Backscattered electron microscope (BSEM) images of accessory minerals from the Belvedere deposit. A) Native gold inclusions in arsenopyrite crystals (GSWA 219551). B) Euhedral baddeleyite crystal from the Belvedere dolerite surrounded by thin zircon fringes (GSWA 219544). C) Former crystals of baddeleyite from the Belvedere dolerite which have been replaced by zircon with abundant very fine-grained inclusions (GSWA 219544). D) Anhedral xenotime crystal containing laths of ore-stage muscovite from quartz–carbonate–arsenopyrite veins (GSWA 219549). E) Anhedral xenotime crystal contained within auriferous arsenopyrite from quartz–carbonate–arsenopyrite veins (GSWA 219551). F) Elongate clusters of xenotime at the margins of a quartz clast from crenulated schist that is locally cross cut by the Belvedere dolerite (GSWA 219539). Abbreviations: asp = arsenopyrite, Au = gold, bd = baddeleyite, chl = chlorite, ga = galena, mu = muscovite, qtz = quartz, xt = xenotime, and zr = zircon.

**Table 1**
SHRIMP operating parameters for all analytical sessions.

| Session date | Mount ID | Sample ID | Target mineral | Kohler aperture (µm) | spot (approx. µm) | $O_2^-$ primary (nA) | M/ΔM (1%) | # scans |
|---|---|---|---|---|---|---|---|---|
| 15–05-2017 | IF1702 | 219,544 | Baddeleyite | 50 | 10 | 0.4–0.6 | 4925.6 | 7 |
| 29–10-2016 | IF1604 | 219,539 | Xenotime | 30 | 10 | 0.3 | 5231.3 | 8 |
| 02–05-2017 | IF1703 | 219,539 (A-D) | Xenotime | 30 | 10 | 0.2–0.3 | 4794.3 | 7 |
| 28–10-2016 | IF1606 | 219,549 (A-H) | Xenotime | 30 | 10 | 0.3 | 5231.3 | 8 |
| 28–29/10/2016 | IF1606 | 219,551 (I-K) | Xenotime | 30 | 10 | 0.3 | 5231.3 | 8 |
| 12–07-2017 | IF1607 | 219551(A,E1-1,H,G) | Xenotime | 30 | 10 | 0.6 | 5161.8 | 8 |
| 12–07-2017 | IF1607 | 219551(B,I,E2-1) | Xenotime | 30 | 10 | 0.2 | 5161.8 | 8 |

**Table 2**
SHRIMP analytical results for baddeleyite from sample GSWA 219544: Belvedere dolerite.

| GSWA 219,544 Belvedere Dolerite Dyke | | | | | | | | | | | | | | |
|---|---|---|---|---|---|---|---|---|---|---|---|---|---|---|
| Mount No. | Grain spot | U (ppm) | Th (ppm) | Th/U | f206 (%) | $^{207}Pb^*/^{206}Pb^*$ | ± 1σ | $^{206}Pb^*/^{238}U$ | ± 1 σ | $^{207}Pb^*/^{235}U$ | ± 1 σ | Dis (%) | $^{207}Pb^*/^{206}Pb^*$ age (Ma) | ± 1 σ (Ma) |
| *Crystallization (2082 ± 30 Ma)* | | | | | | | | | | | | | | |
| 1702 | G.2-1 | 118 | 5 | 0.04 | 1.04 | 0.1351 | 0.0044 | 0.369 | 0.009 | 6.88 | 0.27 | 6 | 2165 | 56 |
| 1702 | B.2-1 | 158 | 4 | 0.02 | −0.16 | 0.1332 | 0.0031 | 0.320 | 0.006 | 5.88 | 0.17 | 16 | 2141 | 41 |
| 1702 | G.1-3 | 107 | 6 | 0.06 | −0.22 | 0.1311 | 0.0037 | 0.320 | 0.013 | 5.78 | 0.28 | 15 | 2113 | 50 |
| 1702 | G.1-1 | 124 | 5 | 0.04 | 0.10 | 0.1299 | 0.0035 | 0.329 | 0.014 | 5.89 | 0.29 | 13 | 2097 | 47 |
| 1702 | G.1-2 | 129 | 3 | 0.02 | 0.45 | 0.1280 | 0.0044 | 0.323 | 0.007 | 5.70 | 0.22 | 13 | 2071 | 60 |
| 1702 | B.1-1 | 209 | 16 | 0.08 | 1.27 | 0.1278 | 0.0073 | 0.319 | 0.006 | 5.63 | 0.34 | 14 | 2068 | 101 |
| 1702 | A.1-1 | 251 | 8 | 0.03 | 0.10 | 0.1277 | 0.0025 | 0.364 | 0.006 | 6.40 | 0.15 | 3 | 2066 | 34 |
| 1702 | B.2-2 | 132 | 3 | 0.02 | 0.52 | 0.1277 | 0.0035 | 0.323 | 0.006 | 5.69 | 0.18 | 13 | 2066 | 48 |
| 1702 | D.1-1 | 231 | 46 | 0.20 | 0.75 | 0.1267 | 0.0034 | 0.349 | 0.006 | 6.09 | 0.19 | 6 | 2053 | 48 |
| 1702 | J.1-1 | 118 | 4 | 0.03 | 1.52 | 0.1223 | 0.0049 | 0.367 | 0.007 | 6.19 | 0.27 | -1 | 1989 | 71 |
| 1702 | E.1-1 | 152 | 6 | 0.04 | 0.96 | 0.1221 | 0.0041 | 0.413 | 0.015 | 6.95 | 0.34 | -12 | 1988 | 60 |
| *Younger statistical outliers* | | | | | | | | | | | | | | |
| 1702 | B.2-3 | 215 | 7 | 0.03 | 0.41 | 0.1207 | 0.0026 | 0.337 | 0.007 | 5.62 | 0.16 | 5 | 1966 | 39 |
| 1702 | E.1-2 | 158 | 8 | 0.05 | 1.09 | 0.1206 | 0.0034 | 0.357 | 0.008 | 5.94 | 0.21 | 0 | 1965 | 51 |
| *High common lead* | | | | | | | | | | | | | | |
| 1702 | I.1-1 | 73 | 8 | 0.11 | 2.63 | 0.1295 | 0.0073 | 0.375 | 0.010 | 6.69 | 0.42 | 2 | 2091 | 99 |
| 1702 | H.1-1 | 101 | 5 | 0.05 | 2.44 | 0.1100 | 0.0065 | 0.372 | 0.008 | 5.64 | 0.35 | -13 | 1799 | 107 |

Pb* indicates radiogenic Pb.

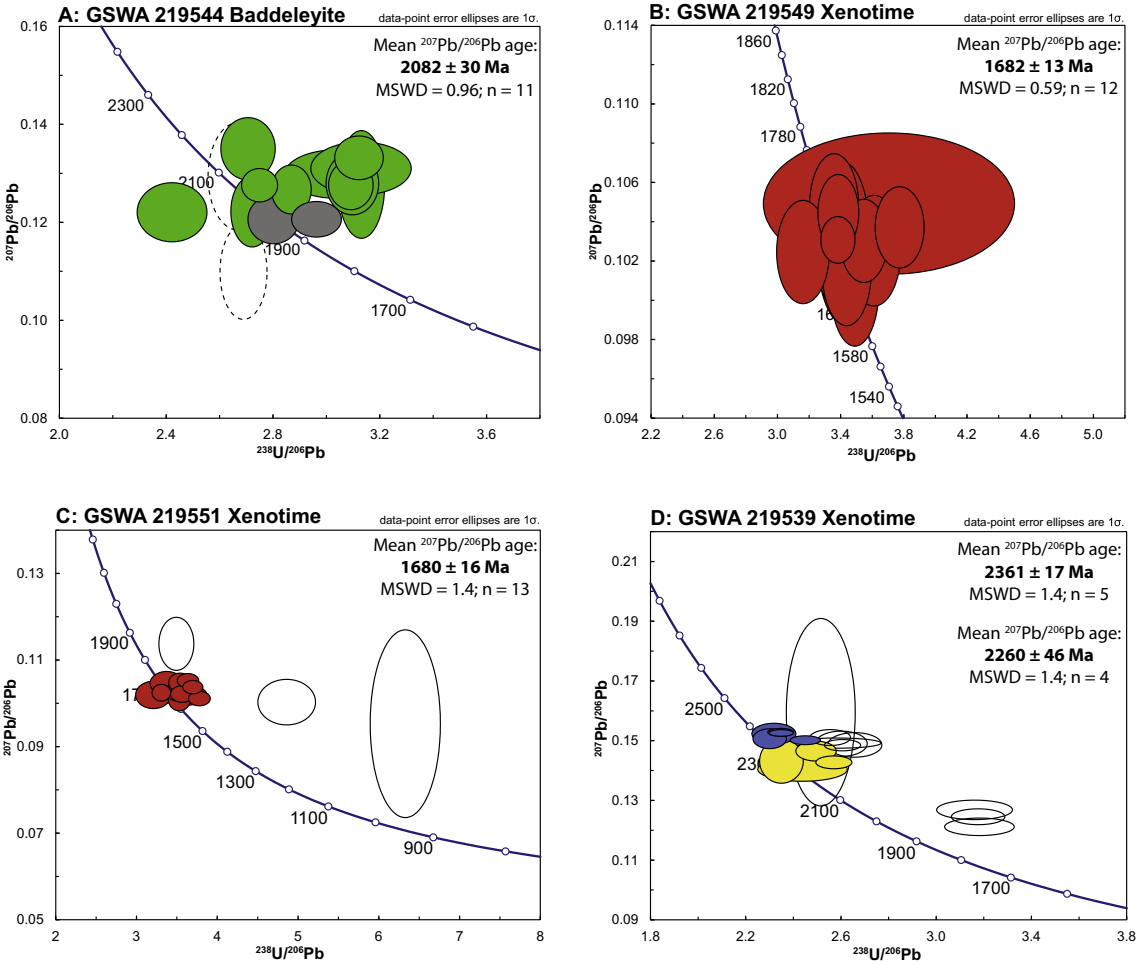


**Fig. 5.** Tera-Wasserburg concordia diagrams of U–Pb data for baddeleyite and xenotime. A) Baddeleyite from the Belvedere dolerite (GSWA 219544). B) Xenotime containing laths of ore-stage muscovite within auriferous quartz-carbonate-sulfide vein (GSWA219549), data with high common lead is not plotted, refer to Table. 3 for analysis details. C) Xenotime intergrown with ore-stage muscovite and auriferous arsenopyrite within auriferous quartz-carbonate-sulfide vein (GSWA219551). D) Xenotime within a crenulated muscovite schist that is locally cross cut by the Belvedere dolerite (GSWA 219539). Key: Dark-coloured ellipses (green = c. 2080 Ma, red = c. 1680 Ma, blue = c. 2360 Ma, yellow = c 2260 Ma) show data used in the age calculations; other ellipses are for inferior data (solid grey = young outliers, dashed ellipses = high common Pb, open black ellipses = discordant data).

**Table 3**
SHRIMP analytical results for xenotime from sample GSWA 219549: Belvedere mineralization.

| GSWA 219,549 Belvedere mineralization | | | | | | | | | | | | | | | | |
|---|---|---|---|---|---|---|---|---|---|---|---|---|---|---|---|---|
| Mount No. | Grain spot | U (ppm) | Th (ppm) | Th/U | f206 (%) | $^{207}Pb^*/^{206}Pb^*$ | ± 1 σ | $^{206}Pb^*/^{238}U$ | ± 1 σ | $^{207}Pb^*/^{235}U$ | ± 1 σ | $^{208}Pb^*/^{232}Th$ | ± 1 σ | Dis (%) | $^{207}Pb^*/^{206}Pb^*$ age (Ma) | ± 1 σ (Ma) |
| *Hydrothermal mineralization (1682 ± 13 Ma)* | | | | | | | | | | | | | | | | |
| 1606 | B.1-1 | 482 | 49 | 0.10 | 0.00 | 0.1049 | 0.0020 | 0.270 | 0.038 | 3.90 | 0.56 | 1.512 | 0.009 | 10 | 1713 | 36 |
| 1606 | B.1-2 | 471 | 58 | 0.12 | −0.14 | 0.1048 | 0.0016 | 0.298 | 0.009 | 4.30 | 0.15 | 1.593 | 0.010 | 2 | 1710 | 29 |
| 1606 | D.2-1 | 931 | 59 | 0.06 | −0.11 | 0.1045 | 0.0012 | 0.295 | 0.007 | 4.26 | 0.12 | 1.640 | 0.010 | 2 | 1705 | 20 |
| 1606 | C.1-2 | 788 | 63 | 0.08 | −0.09 | 0.1037 | 0.0012 | 0.265 | 0.007 | 3.79 | 0.11 | 1.456 | 0.009 | 10 | 1692 | 22 |
| 1606 | G.1-1 | 2611 | 59 | 0.02 | 0.05 | 0.1031 | 0.0007 | 0.296 | 0.006 | 4.21 | 0.09 | 3.305 | 0.010 | 1 | 1681 | 12 |
| 1606 | C.1-1 | 700 | 62 | 0.09 | −0.05 | 0.1030 | 0.0013 | 0.282 | 0.008 | 4.00 | 0.12 | 1.154 | 0.010 | 5 | 1680 | 23 |
| 1606 | H.1-1 | 595 | 64 | 0.11 | 0.58 | 0.1029 | 0.0025 | 0.293 | 0.010 | 4.15 | 0.18 | 0.581 | 0.010 | 1 | 1678 | 46 |
| 1606 | B.1-3 | 508 | 59 | 0.12 | 0.15 | 0.1025 | 0.0017 | 0.277 | 0.009 | 3.91 | 0.14 | 1.333 | 0.009 | 6 | 1671 | 31 |
| 1606 | C.2-1 | 1771 | 58 | 0.03 | 0.55 | 0.1025 | 0.0016 | 0.317 | 0.011 | 4.47 | 0.17 | 2.123 | 0.011 | -6 | 1669 | 29 |
| 1606 | B.1-4 | 462 | 56 | 0.12 | 0.22 | 0.1024 | 0.0018 | 0.294 | 0.009 | 4.15 | 0.15 | 1.494 | 0.010 | 0 | 1669 | 33 |
| 1606 | E.1-1 | 539 | 63 | 0.12 | 0.20 | 0.1016 | 0.0017 | 0.291 | 0.009 | 4.07 | 0.14 | 0.677 | 0.010 | 0 | 1653 | 32 |
| 1606 | B.1-5 | 561 | 59 | 0.10 | 0.39 | 0.1006 | 0.0018 | 0.287 | 0.008 | 3.98 | 0.14 | 0.949 | 0.010 | 1 | 1636 | 33 |
| *High common lead* | | | | | | | | | | | | | | | | |
| 1606 | D.1-1 | 2611 | 53 | 0.02 | 8.05 | 0.1478 | 0.0339 | 0.261 | 0.019 | 5.33 | 1.36 | 4.076 | 0.006 | 35 | 2320 | 393 |

mineralization.

### 6.2.2. GSWA 219551: Auriferous quartz–carbonate–arsenopyrite vein

A second mineralized sample with a Au grade of 4.81 ppm was taken from diamond drill hole PBERCD0045 between 79.2 and 79.68 m. The sample is a quartz–carbonate–arsenopyrite vein containing coarse-grained, euhedral arsenopyrite and associated muscovite–ankerite–rutile alteration. Xenotime crystals are anhedral, < 60 μm in size and commonly contain inclusions of, or is intergrown with, ore-stage alteration products such as muscovite. Inclusions of gold (Fig. 4A), and small inclusions of anhedral xenotime (< 30 μm; Fig. 4E) occurs within arsenopyrite suggesting crystallization of gold, xenotime and arsenopryite was simultaneous.

Sixteen analyses were conducted on 12 xenotime crystals with U and Th concentrations ranging from 141 to 2105 ppm and 50 to 1446 ppm, respectively. Three analyses were excluded from the age determination due to > 10% discordance. The remaining 13 analyses yielded a weighted mean $^{207}Pb*/^{206}Pb*$ date of 1680 ± 16 Ma (MSWD = 1.4; Table 4; Fig. 5C). Since xenotime is contained with auriferous arsenopyrite and intergrown with ore-stage alteration minerals, this date is interpreted to represent the timing of hydrothermal activity associated with gold mineralization.

As the age determinations for samples GSWA 219,549 and 219,551 are indistinguishable within analytical uncertainty, the data have been pooled to provide a more precise weighted mean $^{207}Pb*/^{206}Pb*$ date of 1681 ± 9 Ma (MSWD = 0.96) interpreted to represent the timing of hydrothermal activity related to ore-stage alteration and gold mineralization.

### 6.2.3. GSWA 219539: Crenulated muscovite schist

A very fine-grained, laminated and crenulated muscovite schist that is locally cross cut by the north-trending dolerite dykes was collected from a 2 m-wide outcrop located ~200 m west of the Belvedere deposit (Fig. 3). The sample contains muscovite, quartz, and trace amounts of rutile, monazite and xenotime. Aggregates of very fine-grained monazite occur throughout the rock but are too small to be analysed by ion microprobe. Xenotime crystals are typically small (< 30 μm) and developed as narrow, elongate clusters of crystals up to 10 × 80 μm in, or around the margins of, quartz clasts (Fig. 4F) or as very small (< 10 μm) crystals aligned in the $S_1$ cleavage. Attempts were made to date the xenotime within the cleavage; however, the analyses were discordant because the SHRIMP analysis spot overlapped onto the

**Table 4**
SHRIMP analytical results for xenotime from sample GSWA 219551: Belvedere mineralization.

| GSWA 219,551 Belvedere Mineralization | | | | | | | | | | | | | | | | |
|---|---|---|---|---|---|---|---|---|---|---|---|---|---|---|---|---|
| Mount No. | Grain spot | U (ppm) | Th (ppm) | Th/U | f206 (%) | $^{207}Pb^*/^{206}Pb^*$ | ± 1 σ | $^{206}Pb^*/^{238}U$ | ± 1 σ | $^{207}Pb^*/^{235}U$ | ± 1 σ | $^{208}Pb^*/^{232}Th$ | ± 1 σ | Dis (%) | $^{207}Pb^*/^{206}Pb^*$ age (Ma) | ± 1 σ (Ma) |
| *Hydrothermal mineralization (1680 ± 16 Ma)* | | | | | | | | | | | | | | | | |
| 1606 | J.1–1 | 1261 | 55 | 0.04 | 0.08 | 0.1053 | 0.0010 | 0.275 | 0.007 | 3.99 | 0.10 | 0.506 | 0.009 | 9 | 1720 | 17 |
| 1606 | I.1–2 | 715 | 53 | 0.07 | 0.09 | 0.1049 | 0.0013 | 0.283 | 0.007 | 4.09 | 0.12 | 0.883 | 0.009 | 6 | 1712 | 23 |
| 1607 | A.1–1 | 1201 | 506 | 0.42 | 0.87 | 0.1047 | 0.0017 | 0.296 | 0.012 | 4.28 | 0.18 | 0.097 | 0.010 | 2 | 1709 | 29 |
| 1606 | J.2–2 | 2105 | 57 | 0.03 | 0.15 | 0.1038 | 0.0009 | 0.271 | 0.006 | 3.87 | 0.09 | 1.323 | 0.009 | 9 | 1694 | 16 |
| 1606 | I.1–3 | 580 | 59 | 0.10 | 0.11 | 0.1034 | 0.0015 | 0.282 | 0.008 | 4.02 | 0.13 | 1.124 | 0.010 | 5 | 1685 | 26 |
| 1607 | B.2–1 | 1827 | 1446 | 0.79 | 0.22 | 0.1026 | 0.0017 | 0.306 | 0.015 | 4.33 | 0.22 | 0.101 | 0.010 | −3 | 1671 | 30 |
| 1606 | K.1–1 | 1925 | 54 | 0.03 | 0.52 | 0.1025 | 0.0011 | 0.302 | 0.007 | 4.27 | 0.11 | 2.935 | 0.010 | −2 | 1670 | 21 |
| 1606 | J.3–1 | 1029 | 57 | 0.06 | 0.09 | 0.1024 | 0.0011 | 0.283 | 0.009 | 3.99 | 0.14 | 0.480 | 0.010 | 4 | 1668 | 19 |
| 1606 | I.1–1 | 780 | 61 | 0.08 | 0.04 | 0.1023 | 0.0011 | 0.280 | 0.007 | 3.95 | 0.11 | 1.114 | 0.010 | 4 | 1666 | 21 |
| 1607 | E.2–1 | 848 | 196 | 0.23 | 0.29 | 0.1020 | 0.0019 | 0.312 | 0.014 | 4.39 | 0.22 | 0.095 | 0.011 | −5 | 1661 | 35 |
| 1607 | I.1–1 | 1184 | 335 | 0.28 | 0.06 | 0.1020 | 0.0014 | 0.276 | 0.012 | 3.87 | 0.18 | 0.083 | 0.009 | 6 | 1660 | 25 |
| 1606 | J.2–1 | 1400 | 50 | 0.04 | 0.11 | 0.1012 | 0.0010 | 0.265 | 0.006 | 3.69 | 0.10 | 0.463 | 0.009 | 8 | 1646 | 18 |
| 1606 | I.1–4 | 858 | 61 | 0.07 | 0.00 | 0.1011 | 0.0017 | 0.283 | 0.007 | 3.95 | 0.12 | 1.115 | 0.010 | 2 | 1644 | 31 |
| *Discordance > 10%* | | | | | | | | | | | | | | | | |
| 1607 | G.1–1 | 676 | 634 | 0.94 | 1.79 | 0.1138 | 0.0038 | 0.286 | 0.012 | 4.49 | 0.24 | 0.088 | 0.009 | 13 | 1861 | 60 |
| 1607 | H.1–1 | 141 | 386 | 2.74 | -0.38 | 0.1003 | 0.0033 | 0.206 | 0.010 | 2.85 | 0.17 | 0.065 | 0.007 | 26 | 1630 | 60 |
| 1607 | E.1–1 | 355 | 534 | 1.50 | 15.08 | 0.0954 | 0.0135 | 0.158 | 0.007 | 2.08 | 0.33 | 0.055 | 0.006 | 38 | 1535 | 266 |

**Table 5**
SHRIMP analytical results for xenotime from sample GSWA 219539: Crenulated muscovite schist.

| GSWA 219,539 Crenulated muscovite schist | | | | | | | | | | | | | | | | | |
|---|---|---|---|---|---|---|---|---|---|---|---|---|---|---|---|---|---|
| Mount No. | Grain spot | U (ppm) | Th (ppm) | Th/U | f206 (%) | $^{207}Pb^*/^{206}Pb^*$ | ± 1 σ | $^{206}Pb^*/^{238}U$ | ± 1 σ | $^{207}Pb^*/^{235}U$ | ± 1 σ | $^{208}Pb^*/^{232}Th$ | ± 1 σ | Dis (%) | $^{207}Pb^*/^{206}Pb^*$ age (Ma) | ± 1 σ (Ma) |
| *Main group (2361 ± 17 Ma)* | | | | | | | | | | | | | | | | |
| 1703 | F.1.1 | 2468 | 773 | 0.31 | 0.01 | 0.1522 | 0.0009 | 0.426 | 0.007 | 8.94 | 0.15 | 0.103 | 0.010 | 3 | 2370 | 10 |
| 1703 | C.2–1 | 2854 | 2591 | 0.91 | 0.01 | 0.1519 | 0.0008 | 0.426 | 0.006 | 8.92 | 0.14 | 0.119 | 0.010 | 3 | 2368 | 9 |
| 1604 | A.1–1 | 3398 | 63 | 0.02 | 0.95 | 0.1516 | 0.0021 | 0.431 | 0.011 | 9.01 | 0.27 | 4.238 | 0.010 | 2 | 2364 | 24 |
| 1703 | A.2–1 | 1182 | 1429 | 1.21 | 0.36 | 0.1500 | 0.0021 | 0.435 | 0.009 | 8.99 | 0.22 | 0.119 | 0.010 | 1 | 2346 | 24 |
| 1703 | C.1–1 | 2017 | 1449 | 0.72 | −0.01 | 0.1494 | 0.0010 | 0.408 | 0.007 | 8.41 | 0.16 | 0.079 | 0.009 | 6 | 2339 | 11 |
| *Younger group (2260 ± 46 Ma)* | | | | | | | | | | | | | | | | |
| 1604 | A.1–2 | 1549 | 60 | 0.04 | 0.47 | 0.1458 | 0.0020 | 0.401 | 0.009 | 8.06 | 0.22 | 4.422 | 0.009 | 5 | 2297 | 23 |
| 1604 | A.2–1 | 1051 | 58 | 0.06 | 0.35 | 0.1425 | 0.0046 | 0.425 | 0.011 | 8.36 | 0.36 | 2.061 | 0.010 | −1 | 2258 | 55 |
| 1703 | I.1.1 | 1171 | 1783 | 1.52 | 0.03 | 0.1421 | 0.0014 | 0.389 | 0.008 | 7.62 | 0.17 | 0.081 | 0.009 | 6 | 2253 | 17 |
| 1604 | A.3–1 | 1291 | 47 | 0.04 | 0.42 | 0.1397 | 0.0024 | 0.410 | 0.021 | 7.90 | 0.43 | 2.577 | 0.010 | 0 | 2224 | 30 |
| *Discordance > 7%* | | | | | | | | | | | | | | | | |
| 1703 | D.1.1 | 370 | 517 | 1.40 | 2.26 | 0.1588 | 0.0197 | 0.398 | 0.015 | 8.71 | 1.18 | 0.119 | 0.009 | 12 | 2443 | 210 |
| 1703 | B.1–1 | 1025 | 814 | 0.79 | 0.33 | 0.1503 | 0.0017 | 0.391 | 0.009 | 8.11 | 0.20 | 0.090 | 0.009 | 9 | 2350 | 19 |
| 1604 | B.1–1 | 1983 | 62 | 0.03 | 0.06 | 0.1485 | 0.0008 | 0.387 | 0.019 | 7.93 | 0.39 | 3.611 | 0.009 | 9 | 2329 | 10 |
| 1604 | D.1–1 | 2597 | 58 | 0.02 | 0.14 | 0.1483 | 0.0026 | 0.384 | 0.011 | 7.86 | 0.26 | 3.324 | 0.009 | 10 | 2326 | 30 |
| 1703 | E.1.1 | 405 | 402 | 0.99 | 0.66 | 0.1479 | 0.0026 | 0.376 | 0.011 | 7.67 | 0.26 | 0.126 | 0.009 | 11 | 2322 | 30 |
| 1703 | H.1.1 | 1080 | 662 | 0.61 | 0.17 | 0.1478 | 0.0012 | 0.384 | 0.007 | 7.82 | 0.16 | 0.073 | 0.009 | 10 | 2321 | 14 |
| 1604 | C.1–1 | 362 | 55 | 0.15 | 0.15 | 0.1261 | 0.0020 | 0.316 | 0.011 | 5.50 | 0.21 | 1.524 | 0.009 | 13 | 2044 | 28 |
| 1703 | A.3–1 | 636 | 1503 | 2.36 | 0.24 | 0.1239 | 0.0017 | 0.315 | 0.007 | 5.38 | 0.15 | 0.091 | 0.009 | 12 | 2012 | 24 |
| 1703 | A.1–1 | 391 | 1213 | 3.10 | 0.00 | 0.1205 | 0.0019 | 0.314 | 0.009 | 5.22 | 0.18 | 0.090 | 0.009 | 10 | 1963 | 28 |

surrounding minerals.

Eighteen analyses were made on 17 xenotime crystals with U and Th concentrations ranging from 362 to 3398 ppm and 47 to 2591 ppm, respectively. Five analyses were excluded from the age determination due to > 10% discordance. Of the remaining 13 analyses, two discrete age components are evident with higher U and Th values in grains with the older age mode. The older mode with nine analyses yields a weighted mean $^{207}Pb*/^{206}Pb*$ date of 2350 ± 15 Ma (MSWD = 2.5). However, a more statistically robust date is calculated by excluding data > 7% discordant providing a weighted mean $^{207}Pb*/^{206}Pb*$ date of 2361 ± 17 Ma (MSWD = 1.4; Table. 5; Fig. 5D). The younger mode with four analyses yields a weighted mean $^{207}Pb*/^{206}Pb*$ date of 2260 ± 46 Ma (MSWD = 1.4; Table 5, Fig. 5D). These dates are interpreted to represent xenotime growth during hydrothermal activity at c. 2360 and 2260 Ma.

## 7. Discussion

### 7.1. Host rocks to auriferous quartz–carbonate–arsenopyrite veins

Magmatic baddeleyite within the Belvedere dolerite yielded a crystallization age of 2082 ± 30 Ma, providing a maximum age for the emplacement of the auriferous quartz–carbonate–arsenopyrite veins. This age does not correspond with the timing of other mafic intrusions in either the Capricorn Orogen or the Pilbara region.

### 7.2. Timing of hydrothermal activity and gold mineralization

Three episodes of hydrothermal xenotime growth are recorded at the Belvedere gold deposit: c. 2360, 2260 and 1680 Ma. Xenotime dated at 2361 ± 17 Ma within a crenulated muscovite schist (GSWA 219539) is synchronous with widespread hydrothermal activity throughout the Pilbara region (Pickard, 2002; Rasmussen et al., 2005) and gold mineralization at the Paulsens mine which is related to a cryptic orogenic event (Fielding et al., 2017). However, this event is much older than gold mineralization at the Belvedere deposit, which must be younger than the c. 2080 Ma dolerite host (GSWA 219544). Xenotime from the same sample, dated at 2260 ± 46 Ma, is within uncertainty of monazite growth at 2216 ± 13 Ma from Mount Tom Price, which formed during the early stages of the 2215–2145 Ma Ophthalmia Orogeny (Rasmussen et al., 2005).

Xenotime fully encased in auriferous arsenopyrite and intergrown with ore-stage alteration minerals directly dates the timing of hydrothermal activity and emplacement of the auriferous quartz–carbonate–arsenopyrite veins, thus constraining the timing of gold mineralization to 1681 ± 9 Ma (GSWA 219549 and GSWA 219551). This age is coeval with intracratonic reworking during the earliest stages of the 1680–1620 Ma Mangaroon Orogeny, when medium- to high-grade metamorphism, magmatism and deformation affected rocks of the Gascoyne Province to the south (Sheppard et al., 2005). During this time, major faults throughout the Pilbara region, such as the Nanjilgardy Fault, were reactivated in response to the Mangaroon Orogeny (Fielding et al., 2017; Rasmussen et al., 2007a,b). Reactivation of the Hardey Fault at c. 1680 Ma caused either introduction of new gold or local remobilization of gold at the Paulsens mine (Fielding et al., 2017).

### 7.3. Comparison with the Paulsens gold deposit

The Belvedere and Paulsens gold deposits are situated 6.5 km apart and are associated with the Hardey Fault (Fig. 2), which is a second order splay of the crustal-scale Nanjilgardy Fault. Gold mineralization at both deposits is contained within auriferous quartz–carbonate–-sulfide veins that are hosted in mafic dykes with hydrothermal alteration characterized by muscovite–ankerite–quartz (–rutile) assemblages (Fielding et al., 2017; Thorne and Trendall, 2001). Prior to this study the timing of gold mineralization at the Belvedere deposit was poorly constrained, although ambiguous results from lead-isotope dating of galena suggested that mineralization was late Proterozoic in age (Richards et al., 1981). Thorne and Trendall (2001) attributed gold mineralization at Belvedere and Paulsens to post-Fortescue Group veins, linking their formation to the 1820–1770 Ma Capricorn Orogeny. This age for mineralization is neither supported by field relationships nor geochronological data presented here and by Fielding et al. (2017). Our data show that the ore deposits were not only formed at different times, but have several key differences.

The Paulsens and Belvedere gold deposits are hosted in mafic intrusive rocks. Rheological (and possible chemical) differences between gabbro and surrounding siliciclastic rocks at Paulsens, and dolerite and

surrounding siliciclastic rocks at Belvedere, make them suitable host rocks for gold mineralization. During reactivation of the Hardy Fault, brittle fracturing of the more competent mafic intrusive rocks allowed for emplacement of mineralized quartz-sulfide veins, whereas the surrounding siliciclastic rocks took up the strain as a foliation. Despite both deposits being hosted in mafic intrusive rocks, the mafic rocks themselves differ in type and age. At Paulsens, auriferous quartz–carbonate–sulfide veins are hosted within the pervasively altered Paulsens gabbro, a medium- to coarse-grained, mafic dyke that cuts stratigraphy at a low angle, was deformed during regional-scale $F_1$ folding, and has been overprinted by both $S_1$ and $S_2$ fabrics. Emplacement of the Paulsens gabbro has been precisely dated (U–Pb SHRIMP dating of baddeleyite) at 2701 ± 11 Ma (Fielding et al., 2017). In contrast, auriferous quartz–carbonate–arsenopyrite veins at Belvedere are hosted within the fine- to medium-grained, north-striking Belvedere dolerite that intrudes stratigraphy at a high angle, and which preserves a cleavage in areas where the dolerite is kinked and locally in contact with the mineralized veins. The Belvedere dolerite dyke is much younger, with an igneous crystallization age of 2082 ± 30 Ma (GSWA 219544). Additionally, the deposits are characterized by different sulfide minerals, with Paulsens dominated by pyrite with later pyrrhotite and chalcopyrite (Fielding et al., 2017; Hancock and Thorne, 2016) whereas Belvedere contains arsenopyrite and secondary galena (Fig. 4E).

Field relationships also demonstrate that the north-trending dolerite dykes, including the Belvedere dolerite, cross-cut and offset auriferous quartz–carbonate–sulfide veins at the Paulsens deposit (Fig. 6; Northern Limited Resources Limited, July 2015b). This is supported by U–Pb SHRIMP geochronology on hydrothermal xenotime that indicates that primary gold mineralization at Paulsens occurred at c. 2400 Ma (Fielding et al., 2017), and thus significantly pre-dates the intrusion of the c. 2080 Ma Belvedere dolerite and subsequent mineralization.

### 7.4. Relationship of mineralization to regional orogenic events

When integrated with the tectonothermal framework of the northern Capricorn Orogen (Fielding et al., 2017; Johnson et al., 2013), gold mineralization at Paulsens (c. 2400 Ma) and at Belvedere (c. 1680 Ma) formed during different orogenic events. Fielding et al. (2017) attributed c. 2400 Ma orogenic gold mineralization at Paulsens to a cryptic orogenic event, for which there is evidence of uplift and erosion along the southern Pilbara margin, as well as widespread hydrothermal alteration across the entire Pilbara Craton (Pickard, 2002; Rasmussen et al., 2005). This event is synchronous with the timing of hydrothermal xenotime growth (dated at c. 2360 Ma; GSWA 219539) within a crenulated muscovite schist at Belvedere suggesting this event is a compressional orogeny, however at this stage there is not enough information to understand its full effects.

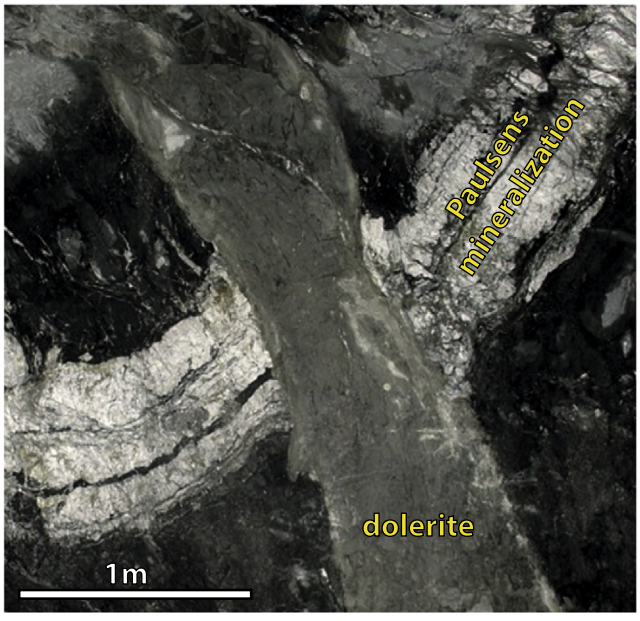


**Fig. 6.** Massive fine-grained dolerite dyke (~1m wide) in the drive wall at the Paulsens gold deposit. The dolerite is part of the same north-trending suite of dykes as the Belvedere dolerite, dated here at c. 2080 Ma. These dykes cross cut and offset auriferous, laminated quartz veins from the Lower mineralized zone at the Paulsens deposit. Level 1095E, face 36 viewed to the southeast.

Gold mineralization at Belvedere, here dated at c. 1680 Ma, is coeval with a second gold mineralizing event at Paulsens (Fielding et al., 2017) that is related to the reactivation of the Nanjilgardy Fault and its second-order structures (including the Hardey Fault) during the earliest stages of the intracratonic 1680–1620 Ma Mangaroon Orogeny (Sheppard et al., 2005). The Mangaroon Orogeny was defined in the Gascoyne Province to the south where its effects are most prominent (Sheppard et al., 2005). In the Gascoyne Province this event is characterized by intraplate extension, high-temperature — low-pressure metamorphism with the synchronous emplacement of voluminous granitic stocks, plutons and batholiths of the 1680–1620 Ma Durlacher Supersuite (Johnson et al., 2017; Sheppard et al., 2005). However, in the northern Capricorn Orogen and Pilbara region the effects of this orogeny are more enigmatic where it lacks evidence for granite magmatism and is of significantly lower metamorphic grade (lowermost greenschist facies). Although the effects of this event are not yet fully known or understood, the event appears to be characterized by the ?strike slip reactivation of major faults and their ancillary structures (Sheppard et al., 2006), which are accompanied by the flow of mineralizing hydrothermal fluids. These structural pathways have played a critical role in the distribution of gold mineralization throughout the region (Fielding et al., 2017; Rasmussen et al., 2007a,b).

### 7.5. Implications for exploration targeting

The presence of closely spaced multiple mineralizing events separated by significant differences in time has important implications for regional-scale exploration targeting. For example, the suite of c. 2080 Ma dolerite dykes is only prospective for c. 1680 Ma gold mineralization since it post-dates the c. 2400 Ma primary gold mineralizing event at Paulsens. In contrast, mafic rocks of the Fortescue and Hamersley Groups were deposited between c. 2775 and 2450 Ma (Arndt et al., 1991; Trendall et al., 2004) which makes them prospective for both c. 1680 and 2400 Ma gold mineralization. Considering that both Paulsens and Belvedere are located in structurally similar areas, and both are associated with mafic dykes, it is the presence of multiple mineralizing events at Paulsens that may account for the difference in gold endowment. Along with a favourable crustal architecture, multiple mineralizing events appear to be required to enrich gold mineralization, thus producing larger, and more economically viable deposits (Meffre et al., 2016). With this understanding, exploration strategies can focus not only on areas with a favourable crustal architecture, but where the rocks are old enough to be overprinted by multiple hydrothermal events. Without knowing the timing of gold mineralization it is possible to erroneously target potential host rocks that have only undergone a minor mineralizing event or that actually post-date all of the mineralizing events in a region or are not in favourable mineralization sites.

## 8. Conclusions

Spatially associated gold occurrences in a geological terrane are commonly thought to have formed during the same mineralizing event (Cheng, 2008; Groves et al., 1998), but this is not the case for the gold deposits from the northern Capricorn Orogen. Here we demonstrate that the Belvedere and Paulsens deposits, which are separated by only 6.5 km, and spatially associated with the same fault (and thus crustal architecture), have different geological histories despite their seemingly

similar appearance. Our results show that mineralized quartz–carbonate–arsenopyrite veins at Belvedere formed at c. 1680 Ma and are hosted within the c. 2080 Ma Belvedere dolerite, whereas the Paulsens deposit is hosted in a c. 2700 Ma mafic sill that was mineralized at c. 2400 Ma. Our results show that despite appearances, the Belvedere and Paulsens gold deposits are not the product of one unique mineralizing event, but formed at different times related to reactivation of major faults.

## Acknowledgement

This project was funded through an ARC linkage grant (LP130100922), the Exploration Incentive Scheme and an industry scholarship by Northern Star Resources as a part of a PhD by I.O.H. Fielding. S.P. Johnson publishes with the permission of the director of the Geological Survey of Western Australia. The SHRIMP II at the John de Laeter Centre at Curtin University was used for all geochronology. We appreciated Sandra Occhipiniti and Andrew Cross for constructive comments which helped to improve the manuscript.

## Appendix

### *Analytical methods*

A primary beam of $O_2^-$ ions was focused through a 50 µm Kohler aperture for baddeleyite and 30 µm Kohler aperture for xenotime, producing an oval 10 µm wide spot on the sample surface with a current of 0.2–0.6nA. The secondary ion system was focused through a 100 µm collector slit onto an electron multiplier to produce mass peaks with flat tops and a mass resolution (1% peak height) of 4795–5230.

Baddeleyite data were collected in sets of 7 scans, with baddeleyite reference material analysed every 3 sample analyses. Xenotime data were collected in sets of 7 or 8 scans, with xenotime reference materials analysed every 4–6 sample analyses. Count times per scan for Pb isotopes 204, background position 204.045, 206, 207, and 208 were 10 s, 10 s, 10 s, 30 s and 10 s, respectively.

Baddeleyite was analysed using the conventional zircon 9-peak run table, calibrated against baddeleyite reference material Phalaborwa (Heaman and LeCheminant, 1993). Instrumental mass fractionation (IMF) in $^{207}Pb/^{206}Pb$ ratios was monitored by repeated analysis of the 3465 Ma OGC zircon standard (OG1 of Stern et al. (2009)). No IMF correction was required since the measured values of OGC were in agreement with the reference value within 2σ uncertainties.

Xenotime was analysed with a 9-peak run table following analytical protocols in Fletcher et al. (2004). Pb/U calibrations and matrix corrections for U and Th contents were based on concurrent measurements of the primary standard MG-1 (Fletcher et al., 2004) and secondary standards z6413 (XENO1) and z6410 (XENO2) (Stern and Rayner, 2003)). Pb/Th was determined indirectly, using a fixed Th/U calibration (Fletcher et al., 2004). Matrix corrections for REE assumed the samples have REE abundances similar to Xeno1.

Raw data from analyses on xenotime were processed using the SQUID 2 add-in (v. 2.50.12.03.08) for Excel 2003 (Ludwig, 2009), and plotted using the ISOPLOT add-in (v. 3.76.12.02.24) (Ludwig, 2003). Common-Pb corrections were based on measured $^{204}Pb/^{206}Pb$ ratios and contemporaneous Pb composition according to the terrestrial Pb evolution model of Stacey and Kramers (1975). Matrix effect corrections were made for all xenotime data using procedures described by Fletcher et al. (2004). All ages are quoted with 95% confidence levels, whereas individual analyses are presented with 1σ errors.

## References

Arndt, N.T., Nelson, D.R., Compston, W., Trendall, A.F., Thorne, A.M., 1991. The age of the Fortescue Group Hamersley Basin, Western Australia, from ion microprobe zircon U-Pb results. Austral. J. Earth Sci. 38 (3), 261–281.

Bierlein, F.P., Groves, D.I., Goldfarb, R.J., Dubé, B., 2006. Lithospheric controls on the formation of provinces hosting giant orogenic gold deposits. Mineral. Depos. 40 (8), 874–886.

Blockley, J. G., 1971, The lead, zinc and silver deposits of Western Australia, in Australia, G. S. o. W., ed., Volume Mineral Resources Bulletin 9: Perth, pp. 237.

Cawood, P.A., Tyler, I.M., 2004. Assembling and reactivating the Proterozoic Capricorn Orogen: lithotectonic elements, orogenies, and significance. Precambr. Res. 128 (3–4), 201–218.

Cheng, Q., 2008. Non-linear theory and power-law models for information integration and mineral resources quantitative assessments. Mathemat. Geosci. 40 (5), 503–532.

Cumming, G.L., Richards, J.R., 1975. Ore lead isotope ratios in a continuously changing earth. Earth Planet. Sci. Lett. 28 (2), 155–171.

Fielding, I.O.H., Johnson, S.P., Zi, J.-W., Rasmussen, B., Muhling, J.R., Dunkley, D.J., Sheppard, S., Wingate, M.T.D., Rogers, J.R., 2017. Using in situ SHRIMP U-Pb monazite and xenotime geochronology to determine the age of orogenic gold mineralization: an example from the paulsens mine. South. Pilbara Crat. Econ. Geol. 112 (5), 1205–1230.

Fletcher, I.R., McNaughton, N.J., Aleinikoff, J.A., Rasmussen, B., Kamo, S.L., 2004. Improved calibration procedures and new standards for U-Pb and Th–Pb dating of Phanerozoic xenotime by ion microprobe. Chem. Geol. 209 (3–4), 295–314.

Forman, F. G., 1938, The Melrose and Belvedere gold mines and vicinity, Mt Stewart Station, Ashburton Goldfields.

Goldfarb, R.J., Groves, D.I., Gardoll, S., 2001. Orogenic gold and geologic time: a global synthesis. Ore Geol. Rev. 18 (1–2), 1–75.

Groves, D.I., Condie, K.C., Goldfarb, R.J., Hronsky, J.M.A., Vielreicher, R.M., 2005. 100th Anniversary special paper: secular changes in global tectonic processes and their influence on the temporal distribution of gold-bearing mineral deposits. Econ. Geol. 100 (2), 203–224.

Groves, D.I., Goldfarb, R.J., Gebre-Mariam, M., Hagemann, S.G., Robert, F., 1998. Orogenic gold deposits: a proposed classification in the context of their crustal distribution and relationship to other gold deposit types. Ore Geol. Rev. 13 (1–5), 7–27.

Hancock, E.A., Thorne, A.M., 2016, Mineralogy of gold from the Paulsens and Mount Olympus deposits, northern Capricorn Orogen: Geological Survey of Western Australia, Record 2016/14, pp. 16

Heaman, L.M., LeCheminant, A.N., 1993. Geochemistry of accessory minerals paragenesis and U-Pb systematics of baddeleyite ($ZrO_2$). Chem. Geol. 110 (1), 95–126.

Hronsky, J.M., Groves, D.I., Loucks, R.R., Begg, G.C., 2012. A unified model for gold mineralisation in accretionary orogens and implications for regional-scale exploration targeting methods. Mineral. Depos. 47 (4), 339–358.

Korsch, R.J., Doublier, M.P., 2016. Major crustal boundaries of Australia, and their significance in mineral systems targeting. Ore Geol. Rev. 76, 211–228.

Johnson, S.P., Korhonen, F.J., Kirkland, C.L., Cliff, J.B., Belousova, E.A., Sheppard, S., 2017. An isotopic perspective on growth and differentiation of proterozoic orogenic crust: from subduction magmatism to cratonization. LITHOS 268–271, 76–86.

Johnson, S.P., Sheppard, S., Rasmussen, B., Wingate, M.T.D., Kirkland, C.L., Muhling, J.R., Fletcher, I.R., Belousova, E.A., 2011. Two collisions, two sutures: Punctuated pre-1950Ma assembly of the West Australian Craton during the Ophthalmian and Glenburgh Orogenies. Precambr. Res. 189 (3–4), 239–262.

Johnson, S.P., Thorne, A.M., Tyler, I.M., Korsch, R.J., Kennett, B.L.N., Cutten, H.N., Goodwin, J., Blay, O., Blewett, R.S., Joly, A., Dentith, M.C., Aitken, A.R.A., Holzschuh, J., Salmon, M., Reading, A., Heinson, G., Boren, G., Ross, J., Costelloe, R.D., Fomin, T., 2013. Crustal architecture of the Capricorn Orogen Western Australia and associated metallogeny. Austral. J. Earth Sci. 60 (6–7), 681–705.

Korhonen, F.J., Johnson, S.P., Wingate, M.T.D., Fletcher, I.R., Dunkley, D.J., Roberts, M.P., Sheppard, S., Muhling, J.R., Rasmussen, B., 2017. Radiogenic heating and craton-margin plate stresses as drivers for intraplate orogeny. J. Metamorp. geol.

Krapež, B., 1999. Stratigraphic record of an Atlantic-type global tectonic cycle in the Palaeoproterozoic Ashburton Province of Western Australia. Austral. J. Earth Sci. 46 (1), 71–87.

Ludwig, K.R., 2003. Isoplot/Ex version 3.00, A geochronological toolkit for Microsoft Excel: Berkeley Geochronology. Centre Special Publication pp. 73.

Ludwig, K.R., 2009. Squid 2.50, a user's manual. Berkeley Geochronology Centre, Berkeley, California, USA pp. 95.

Marston, R. J., 1979, Copper mineralization in Western Australia, in Australia, G. S. o. W., ed., Volume Mineral Resources Bulletin 13 Perth, pp. 227.

Martin, D.M., Morris, P.A., 2010. Tectonic setting and regional implications of ca2.2 Ga mafic magmatism in the southern Hamersley Province, Western Australia. Austral. J. Earth Sci. 57 (7), 911–931.

Martin, D.M., Thorne, A., 2004. Tectonic setting and basin evolution of the Bangemall Supergroup in the northwestern Capricorn Orogen. Precambr. Res. 128 (3), 385–409.

Meffre, S., Large, R.R., Steadman, J.A., Gregory, D.D., Stepanov, A.S., Kamenetsky, V.S., Ehrig, K., Scott, R.J., 2016. Multi-stage enrichment processes for large gold-bearing ore deposits. Ore Geol. Rev. 76, 268–279.

Northern Star Resources Limited, 2015, Northern Star Resources Limited 2015 annual report, (http://www.nsrltd.com/wp-content/uploads/2015/08/NST-Annual-Report-2015-26-8-2015-new-cover1.pdf).

Northern Star Resources Limited, July, 2015, Northern Star Paulsens operations fact sheet, (http://www.nsrltd.com/wp-content/uploads/2015/08/NSR-Paulsens-Operations-Fact-Sheet-July-2015-FINAL.pdf).

Norum, E., 2005, 14 November 2003 to 13 November 2004, Paulsens Project, E08/665, E08/906, E08/1125, E47/977, E47/1134, E47/1135, M08/99, M08/196 and M08/222, Combined Reporting Group C211/1997: Nustar Mining Corporation Limited; Geological Survey of Western Australia Open-file report a070119.

Occhipinti, S.A., Sheppard, S., Passchier, C., Tyler, I.M., Nelson, D.R., 2004. Palaeoproterozoic crustal accretion and collision in the southern Capricorn Orogen: the Glenburgh Orogeny. Precambr. Res. 128 (3–4), 237–255.

Owen, S., 2000, Ashburton Project, Exploration licence 47/902 Belvedere and Tombstone Prospects: Taipan Resources N.L; Geological Survey of Western Australia Open-file report, a61500.
Pickard, A.L., 2002. SHRIMP U-Pb zircon ages of tuffaceous mudrocks in the Brockman iron formation of the Hamersley range Western Australia. Austral. J. Earth Sci. 49 (3), 491–507.
Rasmussen, B., Fletcher, I.R., Muhling, J.R., 2007a. In situ U-Pb dating and element mapping of three generations of monazite: Unravelling cryptic tectonothermal events in low-grade terranes. Geochim. Cosmochim. Acta 71 (3), 670–690.
Rasmussen, B., Fletcher, I.R., Muhling, J.R., Thorne, W.S., Broadbent, G.C., 2007b. Prolonged history of episodic fluid flow in giant hematite ore bodies: evidence from in situ U-Pb geochronology of hydrothermal xenotime. Earth Planet. Sci. Lett. 258 (1–2), 249–259.
Rasmussen, B., Fletcher, I.R., Sheppard, S., 2005. Isotopic dating of the migration of a low-grade metamorphic front during orogenesis. Geology 33 (10), 773–776.
Richards, J.R., Fletcher, I.R., Blockley, J.G., 1981. Pilbara galenas: Precise isotopic assay of the oldest Australian leads model ages and growth-curve implications. Mineral. Depos. 16 (1), 7.
Seymour, D. B., Thorne, A. M., and Blight, D. F., 1988, Wyloo, W.A., (2nd ed.): Western Australia Geological Survey, 1:250 000 Geological Series Explanatory Notes, p. 36.
Sheppard, S., Bodorkos, S., Johnson, S. P., Wingate, M. T. D., and Kirkland, C. L., 2010, The Paleoproterozoic Capricorn Orogeny: intracontinental reworking not continent–continent collision, Volume 108: Geological Survey of Western Australia, Report 108, pp. 33.
Sheppard, S., Farrell, T. R., Bodorkos, S., Hollingsworth, D., Tyler, I. M., and Pirajno, F., 2006, Late Paleoproterozoic (1680–1620 Ma) sedimentation, magmatism and tectonism in the Capricorn Orogen: Geological Survey of Western Australia extended abstracts, pp. 2.
Sheppard, S., Occhipinti, S.A., Nelson, D.R., 2005. Intracontinental reworking in the Capricorn Orogen, Western Australia: the 1680–1620 Ma Mangaroon Orogeny. Austral. J. Earth Sci. 52 (3), 443–460.
Sheppard, S., Occhipinti, S.A., Tyler, I.M., 2004. A 2005–1970 Ma Andean-type batholith in the southern Gascoyne Complex, Western Australia. Precambr. Res. 128 (3–4), 257–277.
Sheppard, S., Rasmussen, B., Muhling, J.R., Farrell, T.R., Fletcher, I.R., 2007. Grenvillian-aged orogenesis in the Palaeoproterozoic Gascoyne Complex, Western Australia: 1030–950Ma reworking of the Proterozoic Capricorn Orogen. J. Metamorp. Geol. 25 (4), 477–494.
Smith, R.E., Perdrix, J.L., Parks, T.C., 1982. Burial Metamorphism in the Hamersley Basin Western Australia. J. Petrol. 23 (1), 75–102.
Stacey, J.S., Kramers, J.D., 1975. Approximation of terrestrial lead isotope evolution by a two-stage model. Earth Planet. Sci. Lett. 26, 207–221.
Stern, R. A., and Rayner, N., 2003, Ages of several xenotime megacrysts by ID-TIMS: potential reference materials for ion microprobe U-Pb geochronology: Radiogenic Age and Isotopic Studies: Report 16: Geological Survey of Canada: Current Research 2003-F1, pp. 7.
Stern, R.A., Bodorkos, S., Kamo, S.L., Hickman, A.H., Corfu, F., 2009. Measurement of SIMS instrumental mass fractionation of Pb isotopes during zircon dating. Geostand. Geoanal. Res. 33, 145–168.
Thorne, A. M., and Seymour, D. B., 1991, Geology of the Ashburton Basin Western Australia, Geological Survey of Western Australia, Bulletin 139, pp. 162.
Thorne, A.M., Trendall, A.F., 2001. Geology of the Fortescue Group, Pilbara Craton, Western Australia, Geological Survey of Western Australia. Bulletin 144, 266.
Trendall, A.F., Compston, W., Nelson, D.R., De Laeter, J.R., Bennett, V.C., 2004. SHRIMP zircon ages constraining the depositional chronology of the Hamersley Group Western Australia. Austral. J. Earth Sci. 51 (5), 621–644.
Tyler, I.M., Thorne, A.M., 1990. The northern margin of the Capricorn Orogen, Western Australia—an example of an Early Proterozoic collision zone. J. Struct. Geol. 12 (5–6), 685–701.
Tyler, I.M., 1991. The Geology of the Sylvania Inlier and the Southeast Hamersley Basin, Geological Survey of Western Australia. Bulletin 138, 124.
White, A.J.R., Smith, R.E., Nadoll, P., Legras, M., 2014. Regional-scale metasomatism in the Fortescue group volcanics Hamersley Basin, Western Australia: implications for hydrothermal ore systems. J. Petrol. 55 (5), 977–1009.
Wingate, M.T.D., Compston, W., 2000. Crystal orientation effects during ion microprobe U-Pb analysis of baddeleyite. Chem. Geol. 168, 75–97.
Wingate, M. T. D., Lu, Y., Blay, O., and Johnson, S. P., 2017a, 206949: dolerite dyke, Tin Hut Bore: Geochronology Record 1432: Geological Survey of Western Australia, pp. 4.
Wingate, M. T. D., Lu, Y., Blay, O., and Johnson, S. P., 2017b, 206953: dolerite sill, Tin Hut Bore: Geochronology Record 1433: Geological Survey of Western Australia, pp. 4.